

PHYSICAL CONDITIONS, GRAIN TEMPERATURES, AND ENHANCED VERY SMALL GRAINS IN BARNARD'S LOOP

CARL HEILES

Astronomy Department, University of California, Berkeley, Berkeley, CA 94720-3411

L. M. HAFFNER AND R. J. REYNOLDS

Astronomy Department, University of Wisconsin, Madison, WI 53706

AND

S. L. TUFTE

Department of Physics, Lewis and Clark College, Portland, OR 97219

Received 1999 November 12; accepted 2000 January 20

ABSTRACT

We derive the radio spectral index of Barnard's loop (BL) from large-scale radio surveys at four frequencies and find it to be a thermal source. We use the radio data together with H α data to determine the electron temperature in BL, the λ Ori H II region, and a high-latitude filament; all of these regions are somewhat cooler than typical H II regions. We perform least-squares fits of the DIRBE diffuse IR intensities to the 21 cm line and radio continuum intensities. After the resolution of a "geometrical conundrum," this allows us to derive the electron density n_e ; we find $n_e \approx 2.0 \text{ cm}^{-3}$ and pressure $P/k \approx 24,000 \text{ cm}^{-3} \text{ K}$. Grains within BL are warmer than in H I regions. Trapped Ly α accounts for the extra heating that is required. This is a general effect that needs to be accounted for in all analyses that examine IR emission from H $^+$ regions. Very small grains that emit 60 μm radiation are enhanced in BL relative to H I by a factor of 2–3, while polycyclic aromatic hydrocarbons that emit 12 μm are probably deficient by a factor of ~ 2 .

Subject headings: dust, extinction — H II regions — ISM: individual (Barnard Loop, λ Orionis)

1. INTRODUCTION

The Wisconsin H α Mapper (WHAM) Sky Survey maps the H α emission from the diffuse warm ionized medium with unprecedented sensitivity and coverage (Haffner, Reynolds, & Tufte 1999). One of the brightest large regions is the Orion-Eridanus superbubble. We have been combining data from many sources for this region to gain a detailed understanding of physical conditions and processes (Heiles, Haffner, & Reynolds 1999). Here we present our results and analysis of a small portion of this region, Barnard's loop (BL).

O'Dell, York, & Henize (1967) developed a coherent physical model based on UV, optical, and radio data. Their UV images are particularly interesting because the UV is dominated by scattered light and allows derivation of dust grain properties; they are also of historical interest, having been taken by astronauts aboard the *Gemini 11* spacecraft. They model BL as an ellipsoid in which the volume density increases roughly as distance², and suggest that the ionized portion of BL is surrounded by a neutral H I shell. They discuss the density structure as being produced by radiation pressure of light from the central stars pushing on the grains. Over a period 3×10^6 yr this would produce the observed structure, which should have expansion velocity $\sim 9 \text{ km s}^{-1}$. We will defer discussion of the kinematics and correspondence with this model to a later paper.

Here we restrict ourselves to a detailed analysis of radio, optical, and diffuse IR emission data to determine the physical conditions and dust grain properties in BL. Section 2 analyzes radio continuum surveys at four different frequencies and finds BL to be a thermal (optically thin free-free) emitter. Section 3 combines the radio and WHAM H α data to derive upper limits on electron temperatures. Section 4 considers a discrepancy between the radio/H α

temperature and previous temperatures derived from the N II and H α lines and derives a correction factor for the absolute intensity scales of the radio and WHAM surveys. Section 5 adopts reddenings and turns the upper limits into actual temperatures. Section 6 combines the DIRBE IR, 21 cm line (Hartmann & Burton 1997), and radio continuum data to derive the BL electron density, grain temperature, and relative population of very small grains and polycyclic aromatic hydrocarbons (PAHs). Finally, § 8 summarizes our findings.

2. RADIO EMISSION: THERMAL OR NONTHERMAL?

Reich (1978) provides a very useful history of radio observations of Barnard's loop (BL), which we will not repeat here. He concludes that there are significant background emission fluctuations, and these prevent an accurate determination of the spectral index of the loop itself. However, Haslam & Salter (1971) studied the bright top portion at 85.5, 240, and 408 MHz and found $T_B \propto \nu^{-2.05 \pm 0.30}$, consistent with a thermal spectrum.

In hopes of narrowing this conclusion, we examined four surveys of radio continuum emission to determine whether BL is a thermal or nonthermal radio emitter. These were the 408 MHz survey of Haslam et al. (1983), the 820 MHz survey of Berkhuijsen (1972), the 1420 MHz survey of Reich & Reich (1986), and the 2326 MHz survey of Jonas, Baart, & Nicolson (1998).¹ Jonas provided us with the full-resolution version of the 2326 MHz survey.

We were concerned that the surveys might exhibit scale errors. We addressed this problem by using the λ Ori H II region as a calibrator, assuming that it was an optically thin

¹ The three lower frequency data sets are available from <http://www.mpifr-bonn.mpg.de/survey.html>.

free-free (thermal) source with $T_B \propto \nu^{-2.1}$. Using this as a calibrator has both good and bad points. Its benefit is that it is large compared with any of the surveys' angular resolution and it is not so bright as to introduce nonlinearities. However, its low intensity makes its derived flux susceptible to zero-level and background intensity fluctuations, which are definitely present, particularly in the lower frequency surveys where nonthermal background radiation is brighter. For each survey we calculated the excess brightness of the H II region for four different choices of ON and OFF regions; our final choice used only the brightest part of the H II region for the ON and two immediately adjacent areas for the OFFs, as shown by the three areas outlined by

dashed lines in Figure 1. We adopted the 2326 MHz survey as a standard and derived the factors required to correct the other surveys to produce the thermal scaling. For the four choices, these factors ranged from 0.99 to 1.98, 0.98 to 1.41, and 1.34 to 1.57 for the 408, 820, and 1420 MHz surveys, respectively; for our final choice illustrated in Figure 1, the factors are 1.61 ± 0.50 , 1.19 ± 0.22 , and 1.45 ± 0.08 . The quoted uncertainties are simply half the difference in ranges quoted above and should be overestimates, because the differences occur primarily because of background fluctuations and our final choice has the OFFs closest to the ON.

If the intensity scales of the surveys were identical, these factors would be unity. The first two have large uncer-

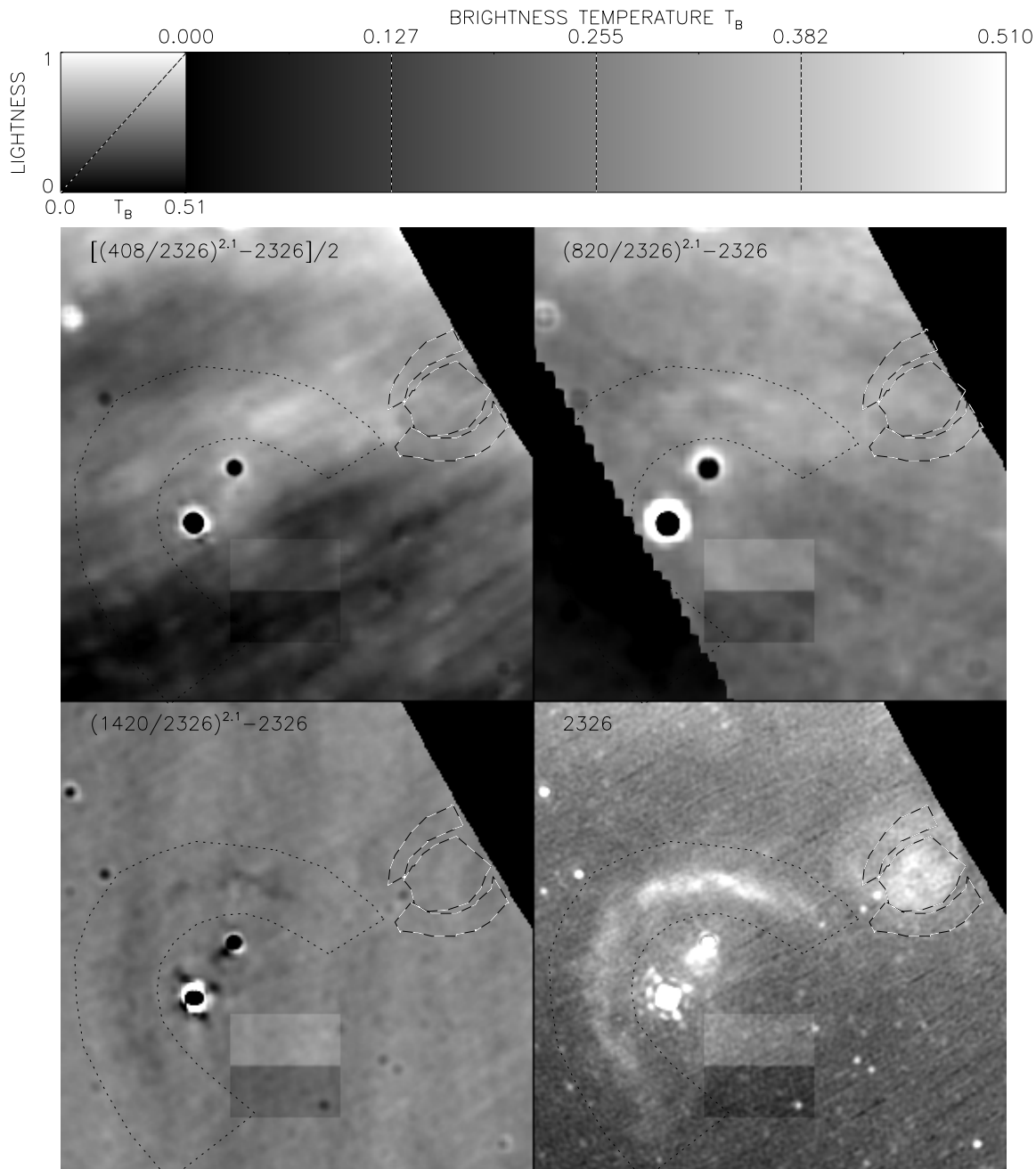


FIG. 1.—Three scaled difference images, with thermal radiation and an arbitrary zero level subtracted away; and the 2326 MHz image, as labeled. Each image is about 26° in size and b increases upward. The two black circles are the Ori A and Ori B H II regions. The dotted line guides the eye to BL; the dashed lines enclose ON and OFF regions for the λ Oph H II region. The rectangles aid the eye in interpreting the gray-scale calibration (see text).

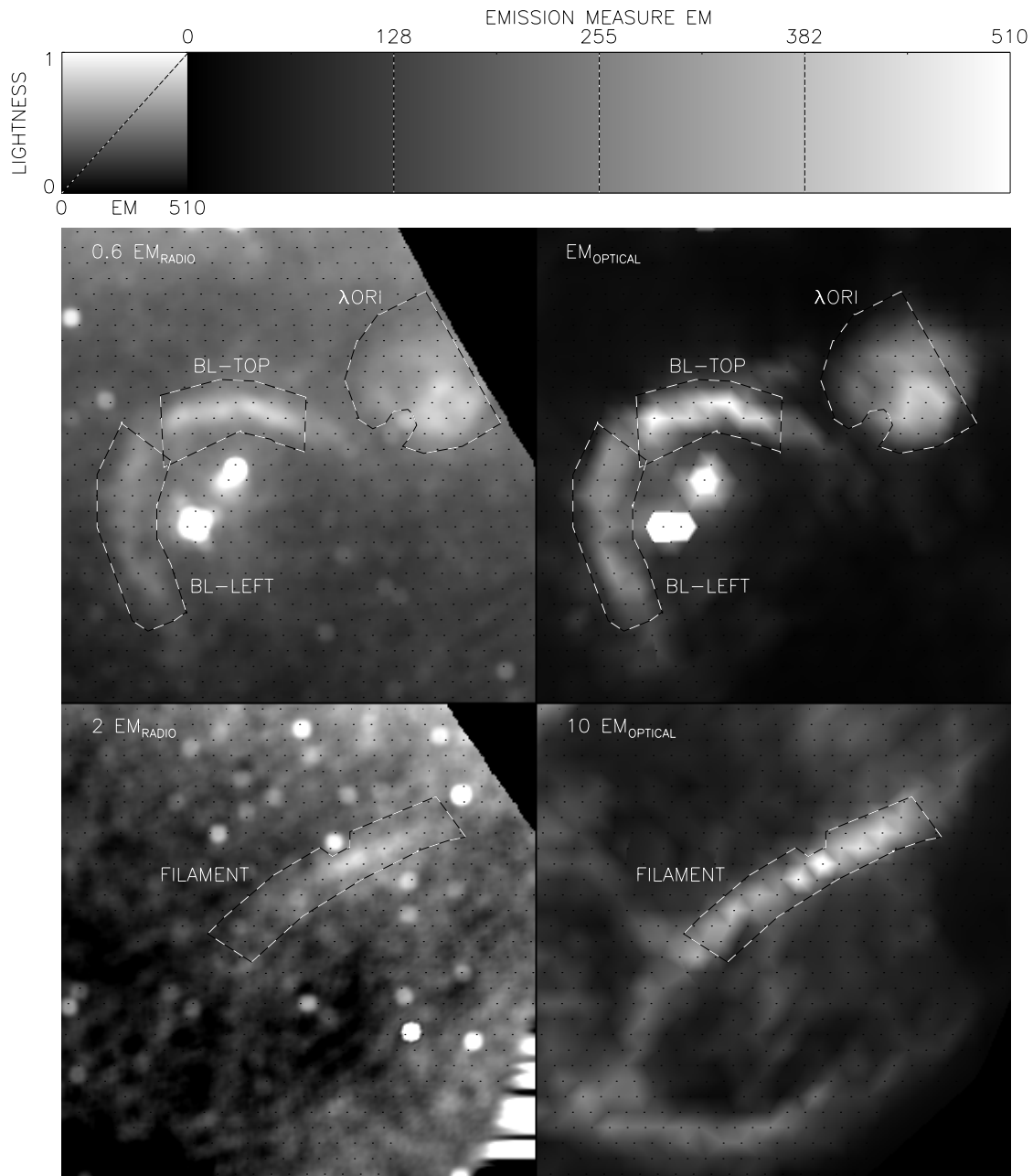


FIG. 2.—Two pairs of 2326 MHz radio and H α optical images side by side; each image is about 26° in size and b increases upward. The upper set exhibits BL and the λ Ori H π region; the two burned-out blobs are Ori A and Ori B. The bottom set exhibits the Filament, which lies near $b = -40^\circ$. The optical data integrate over a 1° diameter circle and are spaced by about 1° ; the positions observed are marked by dots. The dashed lines enclose regions where least-squares fits were done (see text).

tainties but nevertheless seem to differ significantly from unity. The 1420 MHz survey certainly differs significantly from unity. Reich & Reich (1988) find that the 1420 MHz survey needs to be multiplied by 1.55 to agree with the 408 MHz survey; our derived value of 1.45 differs from this factor by only 6%.

We used these factors to make difference images. First we multiply each of the three low-frequency surveys by its factor. Then we multiply each survey image by the factor $(\nu/2326 \text{ MHz})^{2.1}$, which converts all the temperatures to the 2326 MHz temperature if the emission is thermal. Finally, we convolve the 2326 MHz image to the same angular resolution and subtract it. The result is a difference image in which departures from the arbitrary and unknown zero-

level offset represent nonthermal emission. If there is any morphological structure in the difference images that looks like the BL, then the loop exhibits nonthermal emission.

Figure 1 exhibits the three scaled difference images, together with the 2326 MHz image. The diagonal cutoffs in the images arise from the declination limits of the surveys. The dotted half-ring guides the eye to BL, and the calibration rectangles illustrate offsets ± 0.05 K from each difference image. All four images exhibit stripes; they run along the scanning direction and represent zero-level errors from one scan to another in the original data. The three lower frequency difference images reveal artifacts and also background intensity fluctuations. The 1420 MHz difference image (*bottom left*) exhibits broad vertical stripes; these

are zero-level errors because they extend all the way to the north celestial pole. The 408 MHz image exhibits fluctuations over a broad angular scale, about $\frac{2}{3}$ the size of the image, or about 8° ; these are not as distinct at 820 MHz and might be partly or wholly spurious.

The λ Ori H II region is invisible in the difference images of Figure 1, which serves as a check on our method. BL is not recognizable in either the 820 or the 408 MHz difference image. The 408 MHz image does exhibit excess emission ~ 0.12 K to upper right of center, but this feature has no morphological relationship to BL. Moreover, there is no obvious evidence of this excess in the 820 MHz map, so the structure might be spurious. BL seems to be dark in the 1420 MHz difference image. However, the most noticeable dark portions lie on the dark broad stripes, so this appearance may be spurious.

The calibration rectangles are easily recognizable at 820 and 1420 MHz, while BL is not. Thus, the nonthermal low-frequency emission from BL ≤ 0.05 K. At 2326 MHz, BL's bright horizontal top portion (BL-top in Fig. 2) has $T_B \sim 0.35$ K and the left vertical portion (BL-left) has $T_B \sim 0.15$ K at 2326 MHz; the limit of ± 0.05 K means that $\leq 15\%$ and $\leq 33\%$ of the emission is nonthermal at the lower frequencies. At 1420 MHz, BL might exhibit a deficiency at this level, but this is contrary to nonthermal emission, which has a steeper spectrum than thermal emission. Therefore, these visual estimates of upper limits on nonthermal emission are quite conservative.

One usually derives the spectral index of a morphologically distinct extended feature by making plots of intensities at many positions at one frequency versus those at a different frequency and performing a least-squares fit. Instead, for each survey we fitted the difference image *diff* to the 2326 MHz brightness T_{2326} . For BL-top we obtained $d_{\text{diff}}/dT_{2326} = 0.58 \pm 0.25$, 0.05 ± 0.01 , and -0.25 ± 0.03 for the 408, 820, and 1420 MHz data, respectively; for BL-left we obtained 1.79 ± 0.03 and -0.34 ± 0.03 for the 408 and 1420 data, respectively. The significant negative slopes for the 1420 data probably reflect the coincidence of BL with the broad stripes, and the significant positive slope for BL-top at 408 MHz is not revealed in the difference image except as a morphologically inconsistent bright blob. In our opinion, these least-squares fits are meaningless because of artifacts and nonthermal emission fluctuations in the low-frequency images.

We conclude that BL exhibits no recognizable nonthermal emission. For BL-left our conservative upper limit is that $\leq 33\%$ of the 408 MHz emission is nonthermal, and for BL-top $\leq 15\%$. Nonthermal brightness temperatures typically $\propto \nu^{-2.7}$, so at 2326 MHz these limits become $\leq 12\%$ and $\leq 4\%$, respectively.

3. $T_{R/H\alpha}$: THE ELECTRON TEMPERATURE FROM RADIO AND H α EMISSION

In this section we derive the electron temperature by comparing the 2326 MHz and H α intensities, assuming that all of the 2326 MHz emission is thermal. The important quantity for these emission processes is the emission measure EM,

$$EM = n_e^2 L, \quad (1)$$

where n_e is the *total* electron density. Electrons come from both H $^+$ and He $^+$, so $n_e = f_{\text{He}^+} n(\text{H}^+)$, where f_{He^+} accounts for the ionized He; below, we argue that $f_{\text{He}^+} = 1$.

Figure 1 compares the radio and optical images. To facilitate quantitative comparison of the radio and H α emission we convert the usual intensity units of brightness temperature and rayleighs to identical units that are close to the emission measure, normalizing to $T_4 = 1$ and $E(B - V) = 0$:

$$EM_{2326} \equiv 1.80 \times 10^3 T_{B,\text{obs}}, \quad (2a)$$

$$EM_{\text{H}\alpha} \equiv 2.74 I_{\text{H}\alpha,\text{obs}}, \quad (2b)$$

where EM is in $\text{cm}^{-6} \text{pc}$, T_4 the electron temperature in units of 10^4 K, and $E(B - V)$ the reddening in magnitudes. These equations derive from Mezger & Henderson (1967) and Haffner et al. (1999), respectively. Here $T_{B,\text{obs}}$ is the observed 2326 MHz brightness temperature and $I_{\text{H}\alpha,\text{obs}}$ the observed integrated line intensity in rayleighs. These differ from the true intensities for two reasons. One is the error in absolute calibration; we define the intensity scale errors by

$$T_{B,\text{true}} = f_{2326} T_{B,\text{obs}}, \quad (3a)$$

$$I_{\text{H}\alpha,\text{true}} = f_{\text{H}\alpha} I_{\text{H}\alpha,\text{obs}}. \quad (3b)$$

The other is angular size, which is discussed below. With these definitions, we have

$$EM = T_4^{0.35} f_{2326} EM_{2326}, \quad (4a)$$

$$EM = T_4^{0.9} f_{\text{He}^+} e^{2.34E(B-V)} f_{\text{H}\alpha} EM_{\text{H}\alpha}. \quad (4b)$$

Here we have used the extinction curve of Savage & Mathis (1979). Internal extinction, which occurs within the emitting region itself, is less effective than external extinction because a significant fraction of the extinction is scattering, and internal extinction does not scatter photons away from the observer (Mathis 1983). We have assumed that the extinction occurs in a foreground cloud sufficiently far from the emitting region that scattered H α photons are lost, so that the standard extinction law applies. If our assumption is invalid, then reddening has less effect than above. Combining equations (4a) and (4b) we have

$$T_{4,R/H\alpha} = \left(\frac{f_{2326} EM_{2326}}{f_{\text{He}^+} f_{\text{H}\alpha} EM_{\text{H}\alpha}} \right)^{1.82} e^{-4.25E(B-V)}. \quad (5)$$

Here the subscript $R/H\alpha$ means that the temperature is determined by combining radio and H α data.

Figure 2 exhibits two sets of the 2326 MHz radio and H α optical images side by side; one set exhibits BL and the other set a weak filament. We delineate four regions with dashed lines: the λ Ori H II region; BL-top, the top bright portion of BL; BL-left, the left dim portion of BL; and Filament, a weak filament lying near $b = -40^\circ$. For each region we make a least-squares fit for coefficients A and B in the equation

$$EM_{2326} = A + B \times EM_{\text{H}\alpha}. \quad (6)$$

Table 1 presents the results, and Figure 3 exhibits plots of EM_{2326} versus $EM_{\text{H}\alpha}$ for the four regions. Table 1 also presents the deduced temperatures $T_{4,R/H\alpha}$ after multiplying the slopes B for the BL and filament entries by $f_s = 1.032$ as described immediately below. It is not appropriate to multiply A by f_s because A is an offset whose value is determined by the background, whose angular scale exceeds 7° .

Equations (3a) and (3b) are not quite correct because of inadequate angular resolution, otherwise known as "beam dilution." The optical data integrate over a 1° diameter circle and are spaced by about 1° ; BL and the λ Ori H II region are larger than 1° in all dimensions, so no correction

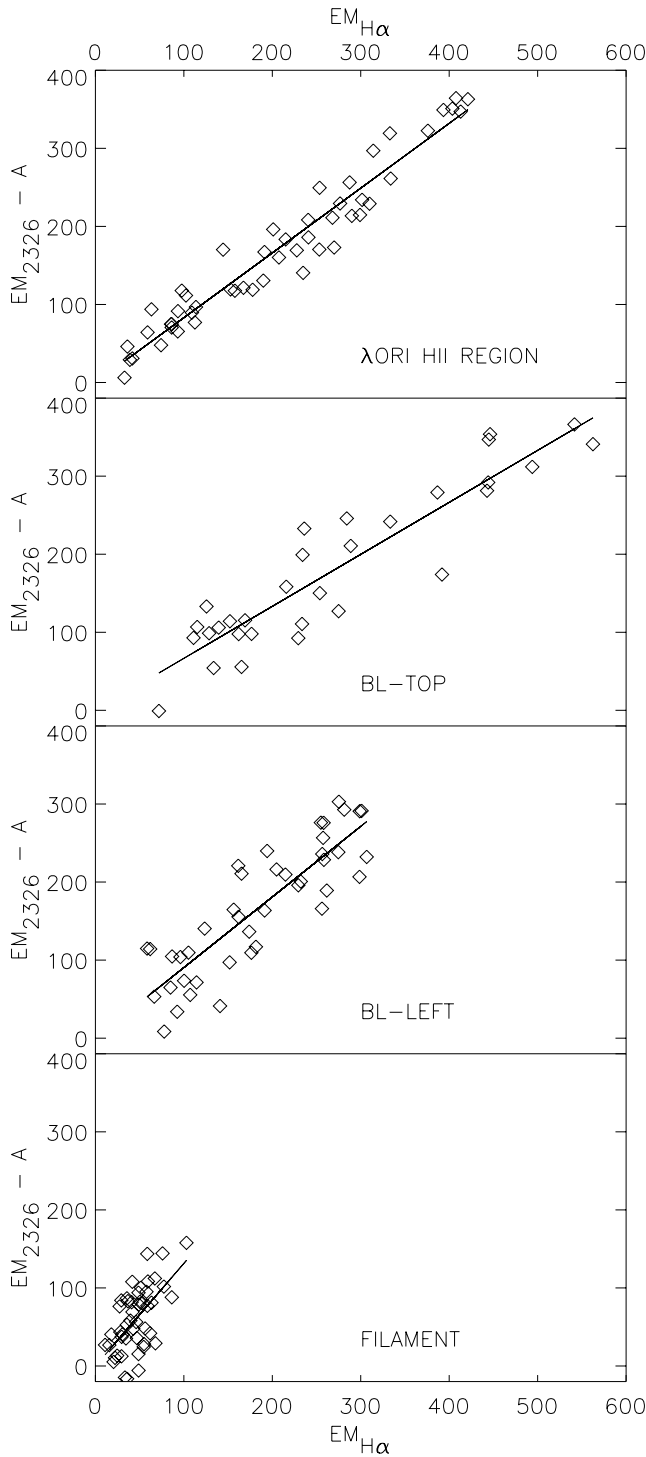


FIG. 3.—Data points and least-squares fits for the four regions shown in Fig. 2.

is required. However, for objects less than 7° diameter the 2326 MHz intensities must be corrected upward by the factor of

$$f_s = \frac{\eta_{\Omega_7}}{\eta_{\Omega_s}}, \quad (7)$$

where η is the beam efficiency, Ω_s the source solid angle, and Ω_7 the solid angle of a 7° diameter circle (Jonas et al. 1998). The λ Ori H II region has diameter $\gtrsim 7^\circ$ so there is no

correction. Using the high-resolution H α image of Isobe (1973), we model BL as a rectangle of dimensions $1.3 \times 7^\circ$, and we take $f_s = (\eta_{\Omega_7}/\eta_{\Omega_{1.3}})^{0.5} = 1.032$, where $\Omega_{1.3}$ is the solid angle of a 1.3 diameter circle.

4. $T_{R/H\alpha}$: CORRECTION FOR ERRORS IN ABSOLUTE CALIBRATION

The accuracy of $T_{R/H\alpha}$ depends on the accuracy of the absolute calibrations of the 2326 MHz and H α data sets. Absolute calibrations are notoriously difficult so we cannot rely on them. Rather, we use other temperature determinations to adjust our results.

Here we consider other temperatures determined by two techniques, both of which compare the [N II] $\lambda 6583$ and H α lines. One uses the line intensity ratio, and one the difference in line width; we denote these temperatures by $T_{N\text{II}/H\alpha}$ and $T_{N\text{II}w\text{id}/H\alpha w\text{id}}$, respectively. Comparing these lines has the great virtue that they are measured with the same instrument, so systematic errors cancel.

4.1. A Two-Temperature Toy Model

The only significant problem from comparing the [N II] and H α lines is possible temperature variations along the line of sight. The [N II] line emissivity increases exponentially with temperature, while the H α and radio emissivities decrease with temperature; thus, the [N II] line preferentially samples high-temperature regions. In a low-density H II region, the equilibrium temperature is independent of density. However, the temperature depends on distance from the star, becoming highest near the edge where the spectrum of ionizing radiation hardens. For example, models 3 and 4 by Rubin (1968) are not too dissimilar from the λ Ori situation and exhibit variations $T_4 \sim 0.45$ to 0.80 . We can get a rough idea of these effects by considering a two-temperature toy model, $T_4 = 0.45$ and 0.80 , with equal emission measures at each temperature. We show the results in Table 2.

For all entries in Table 2, $T_{4,N\text{II}/H\alpha} = 0.630$ and $T_{4,R/H\alpha} = 0.570$. As expected, $T_{N\text{II}/H\alpha} > T_{R/H\alpha}$, but by a modest amount compared with the difference between the physical temperatures of the two regions. In contrast, $T_{N\text{II}w\text{id}/H\alpha w\text{id}}$ depends very sensitively on the relative turbulent velocities in the two regions and can easily lie outside the physical temperature extremes that exist. We conclude that $T_{N\text{II}w\text{id}/H\alpha w\text{id}}$ must be used with caution, unless one can be sure that the nonthermal velocity is constant in the region.

4.2. Temperature Comparisons for Two Regions

Both [N II] and H α lines have been measured for two of our objects, the λ Ori H II region and BL.

4.2.1. λ Ori H II Region

This H II region is excited by the star the O8III star λ Ori; such a star has effective temperature 34,000 K (Binney & Merrifield (1998)). The radius of the He⁺ ionization zone is about 0.35 the H⁺ zone (Osterbrock 1989), so the He⁺ volume is only about 0.04 the H⁺ volume; accordingly, we neglect the He⁺ and take $f_{\text{He}^+} = 1$.

Our upper limit is $T_{4,R/H\alpha} < 0.71 \pm 0.05$. The exciting star has reddening $E(B-V) = 0.12$ mag (Diplas & Savage 1994). If all of this extinction occurs in front of the H II region, then we have $T_{4,R/H\alpha} = 0.43 \pm 0.03$.

Reynolds & Ogden (1982) measured the [N II] and H α lines; applying equation (11) of Haffner et al. (1999) gives

TABLE 1
ELECTRON TEMPERATURES

Region (1)	A (2)	B (3)	$\frac{f_{\text{He}^+}^{1.82} T_{4,R/\text{Hz}}}{e^{-4.25E(B-V)}}$ (4)	$T_{4,R/\text{Hz}} _{\text{corr}}$ (upper limit) (5)	$E(B-V)$ (adopted) (6)	$T_{4,R/\text{Hz}} _{\text{corr}}$ (adopted) (7)
λ Ori	371 ± 7	0.83 ± 0.03	0.71 ± 0.05	$<0.88 \pm 0.06$	0.12	0.53
BL-top	350 ± 15	0.67 ± 0.05	0.49 ± 0.07	$<0.61 \pm 0.09$	0	0.61
BL-left	204 ± 17	0.83 ± 0.14	0.86 ± 0.14	$<1.06 \pm 0.18$	0.13	0.61
Filament	161 ± 13	1.63 ± 0.59	1.68 ± 0.61	$<2.07 \pm 0.75$	0.31	0.55

NOTE.—A and B are results of the least-square fits of EM_{2326} to $\text{EM}_{\text{H}\alpha}$ (eq. [6] and Fig. 3). $T_{4,R/\text{Hz}}|_{\text{corr}}$ in column (5) is identical to column (4), but corrected for intensity scale errors (§ 4); it is an upper limit. Column (6) is the adopted reddening. Column (7) is the actual value of $T_{4,R/\text{Hz}}|_{\text{corr}}$ using the adopted reddening in column (6).

$T_{4,N\text{II}/\text{Hz}} = 0.57 \pm 0.03$. Also, Reynolds & Ogden found $T_{4,N\text{II}w/\text{Hz}w} = 0.60 \pm 0.17$ from a line width comparison; if the uncertainty were smaller, then the agreement would suggest that the temperature does not change much along the line of sight. We adopt the temperature from the intensity ratio, $T_{4,N\text{II}/\text{Hz}} = 0.57 \pm 0.03$.

$T_{4,N\text{II}/\text{Hz}} - T_{4,R/\text{Hz}} = 0.14 \pm 0.04$. The difference is far larger than the uncertainty. However, the results for the toy model in Table 2 suggest that we should expect a difference of a few hundredths.² Suppose that the true value of $T_{4,R/\text{Hz}}$ should be a few hundredths smaller than $T_{4,N\text{II}/\text{Hz}}$, say 0.54.

There are two ways to make our derived $T_{4,R/\text{Hz}}$ equal to 0.54. For one way, the effective $E(B-V)$ is not 0.12 mag, but instead the value required to reduce our upper limit of 0.71 to 0.54; this would make the effective $E(B-V) = 0.06$ mag. This could occur if most of the extinction to the star λ Ori occurs within the H II region itself. This is highly unlikely: the λ Ori H II region has a total column density to its center $N_e \sim 2 \times 10^{20} \text{ cm}^{-2}$ (Reich 1978), which corresponds to $E(B-V) \sim 0.03$ mag for the normal gas/extinction ratio (Bohlin, Savage, & Drake 1978). This is much smaller than the total reddening to the star.

For the other way, we adjust the intensity scale errors to attain agreement. From equation (5) we require $(f_{2326}/f_{\text{H}\alpha})^{1.82} = (0.54 \pm 0.03)/(0.43 \pm 0.03)$, or $f_{2326}/f_{\text{H}\alpha} = 1.13 \pm 0.06$.

4.2.2. BL-Top

Again we take $f_{\text{He}^+} = 1$ because BL is far from the exciting stars. Our upper limit is $T_{4,R/\text{Hz}} < 0.49 \pm 0.07$. There is a

² The difference for the toy model is 0.06, but the toy model considers only two extreme temperatures instead of a continuous distribution and therefore overestimates the difference.

previous radio determination by Gaylard (1984), who measured radio recombination lines and continuum intensities at three positions; the average of his temperatures is $T_{4,R/R} = 0.52 \pm 0.08$. The agreement between our upper limit and his value is good, which implies that the reddening to BL-top is very low.

Reynolds & Ogden (1979) measured the [N II] and H α lines; again, applying equation (11) of Haffner et al. (1999) gives $T_{4,N\text{II}/\text{Hz}} = 0.61 \pm 0.03$. Also, Reynolds & Ogden found $T_{4,N\text{II}w/\text{Hz}w} = 0.76 \pm 0.09$ from a line width comparison. These two temperatures differ by 2 σ . From our discussion in § 4.1 above, we eliminate $T_{4,N\text{II}w/\text{Hz}w}$ from consideration and adopt the temperature from the intensity ratio, $T_{4,N\text{II}/\text{Hz}} = 0.61 \pm 0.03$.

$T_{4,N\text{II}/\text{Hz}} - T_{4,R/\text{Hz}} = 0.12 \pm 0.08$. The difference is significant at the 1.5 σ level. However, it seems that there is temperature structure within BL, so the expected difference is perhaps ~ 0.02 . Thus, we ascribe the larger observed difference to a scale error in $T_{4,R/\text{Hz}}$ and suppose that the true value of $T_{4,R/\text{Hz}}$ should be ~ 0.59 . If there is no extinction, then we must adjust the intensity scale errors to attain agreement. From equation (5) we require $(f_{2326}/f_{\text{H}\alpha})^{1.82} = (0.59 \pm 0.03)/(0.49 \pm 0.07)$, or $f_{2326}/f_{\text{H}\alpha} = 1.11 \pm 0.09$.

4.3. The Final Correction Factor

Above in § 4.2 we found two independent values for the ratio of radio to optical correction factors. They agree well even though their uncertainties are rather large. We adopt the unweighted average $f_{2326}/f_{\text{H}\alpha} = 1.12 \pm 0.07$; the uncertainty does not include the errors in our guesses for the proper differences $T_{4,N\text{II}/\text{Hz}} - T_{4,R/\text{Hz}}$.

We provisionally assign all of the calibration error to $f_{\text{H}\alpha}$, for several reasons. First, the present H α data are not corrected for sky transmission variations, either night-to-night

TABLE 2
TEMPERATURES DERIVED FROM A TWO-COMPONENT TOY MODEL

V_{turb} , Region 1 (1)	V_{turb} , Region 2 (2)	$T_{4,N\text{II}w/\text{Hz}w}$ (3)	V_{turb} (4)	H α Width (5)	N II Width (6)
17	17	0.547	17.19	26.88	21.39
7	7	0.542	7.47	21.91	14.75
12	7	0.678	7.86	23.43	15.10
17	7	0.872	7.96	25.28	15.36
7	12	0.408	11.72	22.37	17.17
7	17	0.210	15.85	22.88	20.05

NOTE.—We assume regions 1 and 2 have equal emission measures with $T_4 = 0.45$ and 0.80, respectively; and $(N/H) = 5.43 \times 10^{-5}$. For all cases, $I_{\text{NII}}/I_{\text{H}\alpha} = 0.229$, $T_{R/\text{Hz}} = 0.570$, and $T_{N\text{II}/\text{Hz}} = 0.630$. Columns (3) and (4) are the temperature and nonthermal line width that would be derived from the observed N II and H α lines. All velocities are half-widths in km s^{-1} .

or airmass. Second, the H α absolute calibration is ultimately tied to the brightness of a 1° diameter region in NGC 7000 (the North America Nebula), and the absolute intensity of this region is uncertain at the level $\sim 12\%$. Finally, L. J. Jonas (1999, private communication) has determined the uncertainty in the 2326 MHz intensity to be $f_{2326} = 1.00^{+0.01}_{-0.05}$.

For the remainder of the present paper, we adopt $f_{2326} = 1$ and $f_{\text{H}\alpha} = 0.89$.

For the ensuing discussion we do not use $T_{4,R/\text{H}\alpha}$. Rather, we use values corrected by the factor $(f_{2326}/f_{\text{H}\alpha})^{1.82} = 1.23$ and denote these corrected values by the symbol $T_{4,R/\text{H}\alpha}|_{\text{corr}}$. These values are listed in Table 1.

5. $T_{R/\text{H}\alpha}$: DISCUSSION FOR INDIVIDUAL OBJECTS

Equation (5) shows that the values for $T_{4,R/\text{H}\alpha}|_{\text{corr}}$ listed in Table 1 are upper limits to the electron temperature because the reddening $E(B-V)$ cannot be negative.

5.1. The λ Ori H II Region

Following our discussion above in § 4.2.1, we assume that all of the extinction occurs in front of the H II region and adopt $E(B-V) = 0.12$. For this choice, our upper limit becomes $T_{4,R/\text{H}\alpha}|_{\text{corr}} = 0.53 \pm 0.04$. By design, this is consistent with $T_{4,N\text{II}/\text{H}\alpha} = 0.57 \pm 0.03$ (§ 4).

This is considerably smaller than typical temperatures of H II regions near the Sun. In particular, the Ori A and Ori B H II regions have measurements of $T_{4,R/R}$ ranging from ~ 0.71 to 0.86 (here the subscript R/R means determined from the ratio of radio recombination lines to radio continuum; see Reifenstein et al. 1970, Shaver et al. 1983). It is also smaller than the *predicted* temperatures: for “standard” abundances, Osterbrock’s (1989) Figure 3.2 should be reasonably representative of the λ Ori H II region and predicts an equilibrium temperature of $T_4 = 0.70$. We now discuss this discrepancy between observed and predicted temperatures for the λ Ori H II region.

The temperature of an H II region is governed primarily by the abundances of nitrogen and oxygen. Lowering the temperature from the predicted $T_4 = 0.70$ to $T_4 = 0.57$ requires that the cooling be increased by a factor of 1.3. To attain the factor 1.3, the [O II] and/or [N II] abundance must increase by the factor 1.8. It is very doubtful that this increase occurs because of an increased gas-phase abundance produced by grain destruction, because Meyer, Cardelli, & Sofia (1997) and Meyer, Jura, & Carfelli (1998) find that only $\sim 30\%$ of the O and $\sim 0\%$ of the N are locked up in grains.

An alternative to the observed temperature being as low as 5700 K is the fraction $[N^+/\text{N}]$ being lower than unity, because the observed value $T_{4,N\text{II}/\text{H}\alpha} = 0.57 \pm 0.03$ relies on the assumption that $N^+/\text{N} = \text{H}^+/\text{H}$ (Haffner et al. 1999). In fact, models by Sembach et al. (2000) suggest that this assumption is incorrect; instead, $N^+/\text{N} = 0.7 \text{H}^+/\text{H}$. If this is correct, then the observed $T_{4,N\text{II}/\text{H}\alpha}$ becomes 0.62 ± 0.03 . This raises the temperature of the λ Ori H II region and makes it closer to, but still different from, the theoretical prediction.

We do not understand the causes for the smaller temperature of the λ Ori H II region.

5.2. BL-Top

Following our discussion above in § 4.2.2, we adopt $E(B-V) = 0$. This makes the temperature equal to our

upper limit, so $T_{4,R/\text{H}\alpha}|_{\text{corr}} = 0.61 \pm 0.09$. Again, by design this is close to $T_{4,N\text{II}/\text{H}\alpha} = 0.61 \pm 0.03$.

5.3. BL-Left

Our upper limit is $T_{4,R/\text{H}\alpha}|_{\text{corr}} < 1.06 \pm 0.18$. This is considerably higher than BL-top. We expect the physical conditions in BL-left and BL-top to be similar because they are part of the same structure; this implies that the true temperature is lower than our raw measurements imply and that extinction is important. If BL-left has the same temperature as BL-top, then equation (5) predicts $E(B-V) = 0.13$ mag.

This set of conditions is entirely in line with the ratio of H α to H β line intensities, which we denote by $R_{\alpha\beta}$. Isobe (1978) presents a map of this ratio from which we estimate

$$\frac{R_{\alpha\beta,\text{BL-top}}}{R_{\alpha\beta,\text{BL-left}}} \sim 0.80, \quad (8)$$

and a good approximation to the ratio of line intensities (Martin 1988) is

$$R_{\alpha\beta,\text{theory}} \approx 2.88 T_4^{-0.1} e^{1.05 E(B-V)}. \quad (9)$$

These, together with the Table 1’s ratio of the slopes B for the two regions, provide an independent estimate of the quantities $T_{\text{ratio}} = T_{4,\text{BL-top}}/T_{4,\text{BL-left}}$ and $E_{\text{diff}} = [E(B-V)_{\text{BL-top}} - E(B-V)_{\text{BL-left}}]$; we obtain $T_{\text{ratio}} \sim 0.58$ and $E_{\text{diff}} \sim -0.19$ mag, which agrees quite well with our above results.

We conclude that BL-left has the same temperature as BL-top, $T_{4,R/\text{H}\alpha} \approx 0.61$. Its reddening $E(B-V) \approx 0.13$ mag corresponds to a foreground $N_{\text{H}} \sim 8.0 \times 10^{20} \text{ cm}^{-2}$.

5.4. Filament

Our upper limit is $T_{4,R/\text{H}\alpha}|_{\text{corr}} < 2.07 \pm 0.75$. The uncertainty is large, but an eyeball examination of Figure 3 persuades us that this value is reliable and is statistically significantly higher than in the other regions.

One spot in this region, $(\alpha, \delta) = (04^{\text{h}}00^{\text{m}}25^{\text{s}}.0)$, was observed by Reynolds & Ogden (1979, entry 3 in Table 1); these data give $T_{4,N\text{II}/\text{H}\alpha} = 0.55 \pm 0.03$. Applying equation (5), we find $E(B-V) \sim 0.31$ mag. This corresponds to $N_{\text{H}} \sim 1.9 \times 10^{21} \text{ cm}^{-2}$, which in turn corresponds to a 100 μm brightness of 28 MJy sr^{-1} for the usual IR to H I conversion of Schlegel, Finkbeiner, & Davis (1998). The observed 100 μm brightnesses are smaller than this, varying from ~ 6 to 13 MJy sr^{-1} . This seeming discrepancy is not meaningful because the H I column density is large and, moreover, the IR emission per H nucleus is ~ 0.7 to $1.1 \text{ MJy sr}^{-1} \text{ cm}_{20}^{-2}$, with the higher ratios correlated with the higher 100 μm brightnesses, which implies the presence of H $_2$. Under these dense conditions, the true column density exceeds that indicated by the IR emission as discussed in § 6.

We adopt the reddening required to make $T_{4,R/\text{H}\alpha}$ match $T_{4,N\text{II}}$, 0.31 mag. This weakens the observed brightness by a factor of ~ 3.7 . From Figure 3, we see that the observed H α brightness is $\text{EM}_{\text{H}\alpha} \sim 90 \text{ cm}^{-6} \text{ pc}$; thus, the unabsorbed brightness $\sim \text{EM}_{\text{H}\alpha} \sim 340 \text{ cm}^{-6} \text{ pc}$. This makes the intrinsic optical brightness of filament ~ 0.6 the optical brightness of BL.

6. DIRBE FITS

IR emission traces the total warm/cold column density $[N(\text{H}_{\text{tot}}) = N(\text{H I}) + 2N(\text{H}_2) + N(\text{H}^+)]$ and 21 cm line

emission traces the H I column density $N(\text{H I})$; thus the appropriately scaled difference traces $[2N(\text{H}_2) + N(\text{H}^+)]$. For H^+ , note the important difference between its IR and $\text{H}\alpha$ (or radio) emission: IR traces column density $N(\text{H}^+)$, while $\text{H}\alpha$ traces emission measure $\text{EM} = N(\text{H}^+)n_e$. This means that the comparison provides n_e .

The important scaling factor is B , the IR emission per hydrogen nucleus. The IR emission peaks near $100 \mu\text{m}$. Global fits at $100 \mu\text{m}$ typically obtain B in the vicinity of $0.65 \text{ MJy sr}^{-1} \text{ cm}_{20}^{-2}$ (Schlegel et al. 1998; Reach, Wall, & Odegard 1998; Heiles et al. 1999). Here we adopt the somewhat lower value 0.62 of Arendt et al. (1998) because they obtained the full DIRBE spectral coverage. Let the emission per nucleus in ionized gas be $b_{\text{H}^+} B$. Then, neglecting H_2 , we have

$$\text{IR}_{\text{obs}} = A + BN(\text{H I}) + b_{\text{H}^+} BN(\text{H}^+). \quad (10)$$

To treat observational data, consider a least-squares fit for the coefficients A , B , and C in the equation

$$\text{IR}_{\text{obs}} = A + BN(\text{H I}) + Cn_e N(\text{H}^+). \quad (11)$$

Here IR_{obs} is the DIRBE data, $N(\text{H I})$ is the integrated 21 cm line intensity, and $N(\text{H}^+)n_e$ is from either the 2326 MHz data or the velocity-integrated $\text{H}\alpha$ line intensity. Comparing the last term in these equations gives

$$n_e = \frac{b_{\text{H}^+} B}{C}. \quad (12)$$

The radio data are better than the optical data for these fits because they have higher angular resolution and are unaffected by extinction; their higher noise is unimportant because BL is intense. The radio and optical data give comparable results. In actual practice we do not fit equation (11) but instead

$$\text{IR}_{\text{obs}} = A + BN(\text{H I}) + C' \text{EM}_{2326}. \quad (13)$$

From equation (4a) it is clear that

$$n_e = T_4^{0.35} f_{\text{He}^+}^{-1} f_{2326} b_{\text{H}^+} \frac{B}{C'} = 0.84 b_{\text{H}^+} \frac{B}{C'}, \quad (14)$$

where the numerical value is for $T_{4,R/\text{H}\alpha}|_{\text{corr}} = 0.61$, $f_{\text{He}^+} = 1$, and $f_{2326} = 1$.

Reliable results require choosing appropriate regions, specifically ones with small $N(\text{H I})$ and no H_2 . High $N(\text{H I})$ regions are unsuitable for three reasons: (1) their possible saturation of the 21 cm line makes it an invalid tracer of $N(\text{H I})$, (2) their associated extinction shields the interior from starlight, making dust grains cooler and reducing the IR emission per H atom, and (3) their probable associated H_2 provides extra dust unrelated to H I, increasing the IR emission per H atom.

6.1. Electron Density and Grain Emission Spectrum

Most of BL does not satisfy the low $N(\text{H I})$ criterion because there are very dense background molecular clouds. Nevertheless, we were able to locate two small portions of BL and its environs where molecular clouds are absent. These regions are outlined by dashed lines in Figure 4, and we shall refer to them as BL=top and BL=bottom. We performed fits at the six relevant DIRBE wavelengths.

Figure 5 exhibits the logarithm of the IR emission in MJy sr^{-1} per $N(\text{H I})_{20}$, where the subscript means units of 10^{20}

cm^{-2} ; this is equal to $\log B$ in equation (13). This figure also shows the global average spectrum determined by Arendt et al. (1998). Our spectrum agrees well with the global one.

At $100 \mu\text{m}$, equation (14) gives $n_e/b_{\text{H}^+} = 0.84 \pm 0.15$ and $1.16 \pm 0.09 \text{ cm}^{-3}$ for the top and bottom regions, respectively. These differ by 1.8σ , which we regard as fair agreement, and we adopt the average $n_e/b_{\text{H}^+} = 1.0 \text{ cm}^{-3}$.

The ratio (C'/B) is the ratio of the H^+ and H I IR spectra; if this ratio depends on wavelength, then the grain emission spectrum differs for ionized and neutral gas. Figure 6 exhibits this ratio as normalized to unity at $\lambda = 100 \mu\text{m}$. The H^+ spectrum differs significantly from the H I spectrum. Relative to $\lambda = 100 \mu\text{m}$, the $60 \mu\text{m}$ points are definitely larger, and the 12 and $240 \mu\text{m}$ points are probably smaller (the errors are large, particularly at $240 \mu\text{m}$).

Our least-squares fit allows us to predict $\text{IR}_{\text{pr}} = A + BN(\text{H I}) + C' \text{EM}_{2326}$. Thus the difference $\text{IR}_{\text{obs}} - \text{IR}_{\text{pr}}$ (in least-squares terminology, the residual) is an approximate measure of $N(\text{H}_2)$ combined with the deviation of n_e from its average, that is,

$$R = \text{IR}_{\text{obs}} - \text{IR}_{\text{pr}} = B \left[2N(\text{H}_2) + N(\text{H}^+) \left(1 - \frac{n_e}{\langle n_e \rangle} \right) \right]. \quad (15)$$

There is also a minor contribution from saturation of the 21 cm line.

The lower right-hand quadrant in Figure 4 maps this difference, which depends on two terms—the “molecular” and “ionized” terms. The ionized term can be positive or negative: it is negative in regions of large n_e , where a small column density gives bright 2326 MHz emission. Thus, dense H II regions would stand out as deficiencies in Figure 4 if they were not associated with molecular clouds. However, the dominant contribution to this image is clearly the Orion molecular clouds, which produce the large, prominent burned-out bright blob.

6.2. The Geometrical Conundrum

Above we adopted $n_e/b_{\text{H}^+} = 1.0 \text{ cm}^{-3}$. The 2326 MHz brightness temperature $\sim 0.13 \text{ K}$, which corresponds to $N(\text{H}^+)n_e = 160 \text{ cm}^{-6} \text{ pc}$. Combining these with $b_{\text{H}^+} = 1$ gives $N(\text{H}^+)_{20} = 5.0$ and path length $L = 160 \text{ pc}$.

This path length is very long: BL is at the distance of Orion, about 450 pc, so our 160 pc line-of-sight length is 36% of the total distance. This, in turn, implies that BL is a cylinder that happens to have its axis accurately pointed toward us. This is not only deeply unsatisfying, but also at odds with what we would expect from the simple geometrical and physical model of a thick-walled spherical shell.

In the vicinity of the fitted regions, BL has radius $R \sim 6^\circ 1$ and apparent thickness $T \sim 1^\circ 3$; these translate to lengths $R = 48$ and $T = 10 \text{ pc}$. Such a shell has a maximum tangential path length through its edge of $L_{\text{sph}} \sim 60 \text{ pc}$. Our derived path length exceeds this by a factor of 2.7; not only that, it exceeds even the diameter by a factor of 1.6! This discrepancy is the geometrical conundrum.

Clumping makes the conundrum even worse. Suppose that the line of sight within BL contains clumps that occupy a fraction f of the sight line. This does not affect any of our derived physical parameters, including L ; however, in this case L refers to the length of the line of sight *within the clumps*. The *total* length within which the clumps lie is L/f . This makes the geometrical conundrum worse by a factor of f .

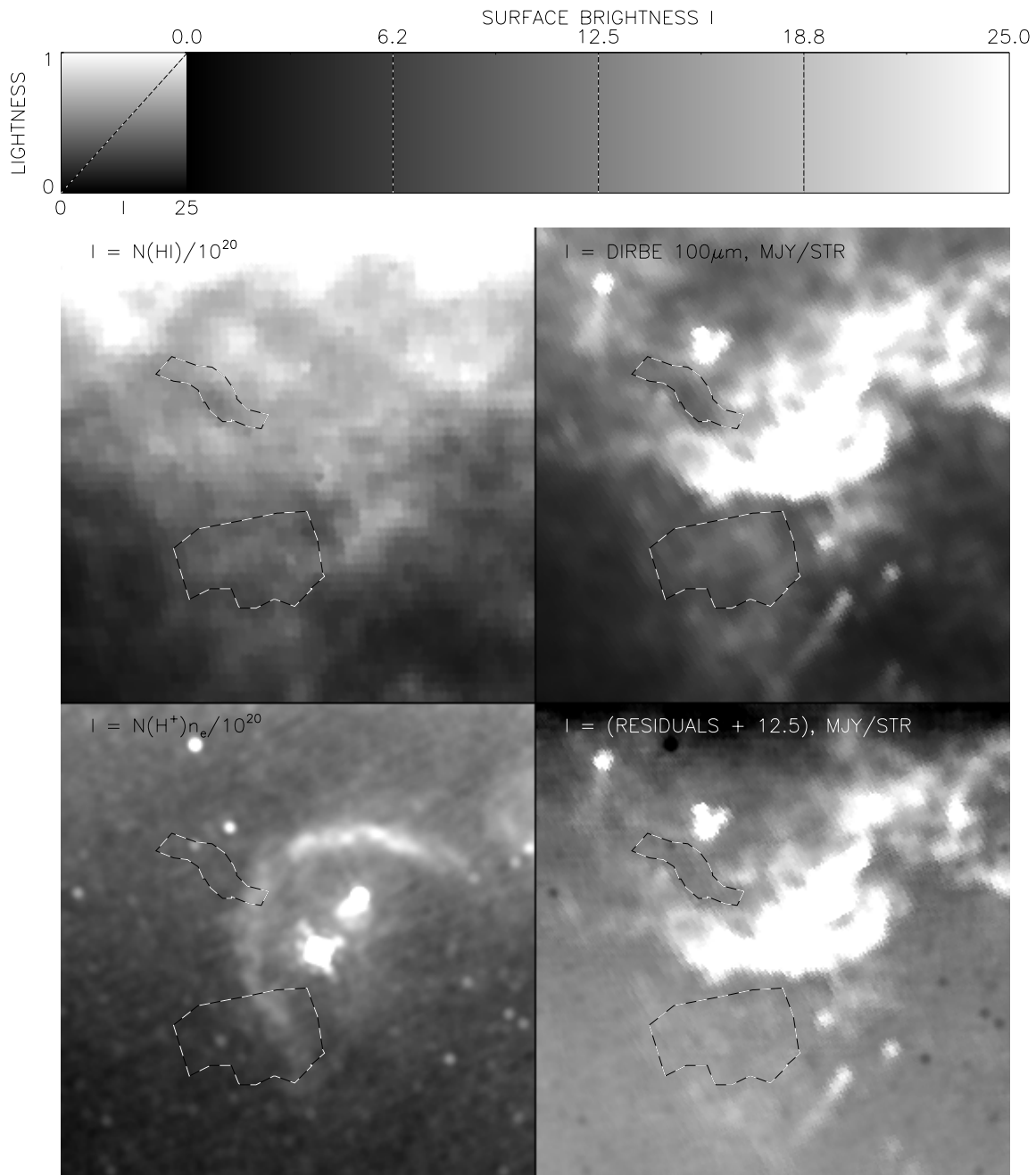


FIG. 4.—Three images of data used for the DIRBE least-squares fits. The dashed lines outline the small regions where background molecular clouds are absent and allow a reasonably accurate least-squares fit of eq. (13). Each image is about 26° in size and b increases upward.

To resolve the conundrum comfortably, we need to decrease L to something less than its maximum of 60 pc. For discussion purposes, we will assume $L = 40$ pc. This means we need to decrease our derived path length by a factor of 4.

Suppose that ionized regions exhibit more grain emission per $N(\text{H}_{\text{tot}})$ than neutral regions; this means $b_{\text{H}^+} > 1$. This increases n_e by the factor b_{H^+} and decreases L by the *square* of b_{H^+} . To resolve the conundrum in a comfortable way, we need $b_{\text{H}^+}^2 \sim 4$ or $b_{\text{H}^+} \sim 2$.

We adopt this as the resolution to the conundrum. Thus, we adopt $n_e = 2.0 \text{ cm}^{-3}$. BL has $T_{4,R/\text{Hz}}|_{\text{corr}} \approx 0.61$; thus, $\tilde{P}_4 \equiv P/10^4 k = 2n_e T_4 \approx 2.4$.

7. THE BL BIG GRAINS ARE WARMER THAN H I BIG GRAINS

Above in § 6.2, we found the geometrical conundrum requires more $100 \mu\text{m}$ IR emission per grain than in H I regions, and we adopted $b_{\text{H}^+} = 2$. And in § 6.1, we found the IR spectrum of BL to be different from that of H I. Both the increased $100 \mu\text{m}$ emission and the changed spectrum suggest that the BL grains are warmer than the H I grains. In the remainder of this section, we will explore this temperature increase. We shall assume that the *number* of $100 \mu\text{m}$ emitting grains per H nucleus is identical in BL and H I regions.

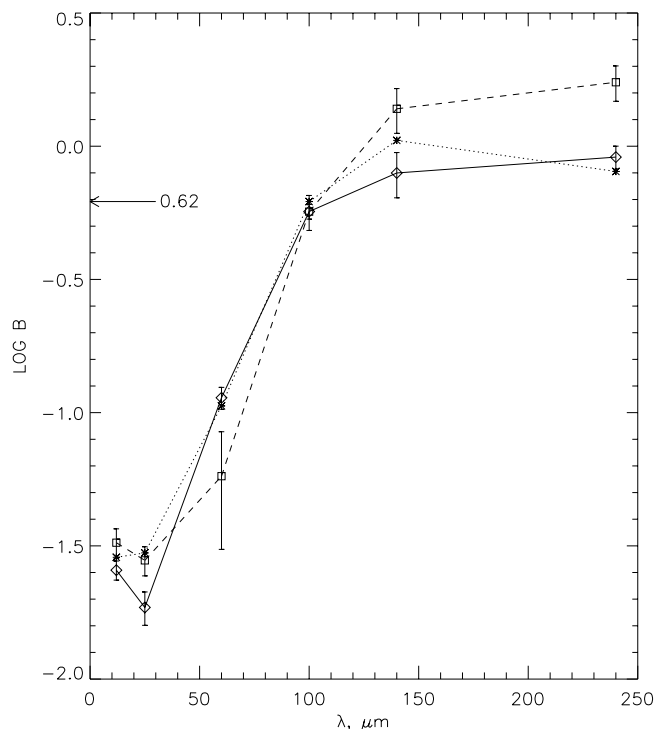


FIG. 5.— B is the logarithm of the IR brightness (MJy sr^{-1}) per 10^{20} H nuclei in the neutral gas; the arrow marks the global average. Dashed and solid lines are for the top and bottom regions in Fig. 4, respectively; the dotted line and global average are from Arendt et al. (1998).

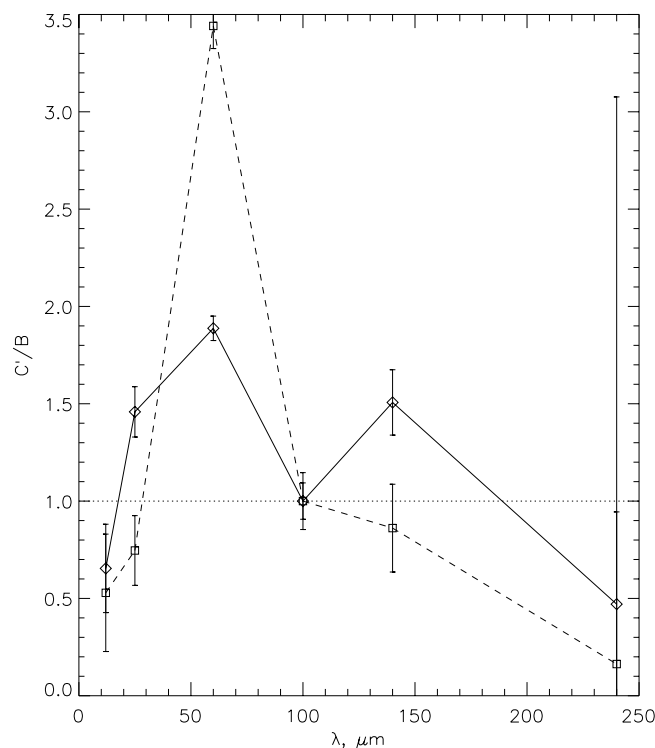


FIG. 6.— (C'/B) , which is the ratio of the H^+ and H I IR spectra, normalized to unity at $\lambda = 100 \mu\text{m}$. Dashed and solid lines are for the top and bottom regions in Fig. 4, respectively; the dotted line is the global average of Arendt et al. (1998). If we had derived n_e at wavelengths other than $100 \mu\text{m}$, the derived n_e would equal B/C' times the $100 \mu\text{m}$ value.

We perform least-square fits of the IR spectrum to determine the big grain temperature T_{BG} . In all fits we use a v^2 emissivity law and weight the points by the inverse square of the uncertainties. In H I regions, the $\lambda \gtrsim 100 \mu\text{m}$ radiation comes almost exclusively from big grains (BGs) and $60 \mu\text{m}$ radiation from very small grains (VSGs; Désert, Boulanger, & Puget 1990). These are two distinct grain populations and in solving for the temperature of $\lambda = 100 \mu\text{m}$ emitting grains we must consider only the BGs, that is, we must use IR intensities for $\lambda \geq 100 \mu\text{m}$. For the three H I grain spectra in Figure 5 we obtain $T_{\text{BG}} = 18.2, 15.4$, and 17.5 K for the global, top, and bottom regions, respectively. These refer to H I regions. The uncertainties on our derived temperatures (top, bottom) are large, so below we will use the global $T_{\text{BG}} = 18.2$ K as a reference.

In BL, Figure 6 shows $60 \mu\text{m}$ is much stronger than in H I regions by a factor of 1.9 to 3.4. This can occur for two reasons. One, the population of VSGs is enhanced in BL relative to H I regions. Two, the temperature of BGs is considerably larger in BL than in H I regions.

Below, we will least-squares fit the grain temperatures to the IR spectra for the H^+ in BL (top, bottom) and exhibit the results in Table 3. The table also displays two important related quantities. One is b_{H^+} , the ratio of the $100 \mu\text{m}$ emissivity at the derived T_{BG} in BL to that in the global H I. The other is $T_{\text{BG}}/(T_{\text{BG,H I}})^6$: for a grain emissivity $\propto v^2$, this is the expected ratio of grain heating (equal to total grain IR emission).

To begin, we suppose that the enhanced $60 \mu\text{m}$ intensity in BL comes from BGs that are warm enough to overwhelm the VSG emission. Therefore, in this fit we derive T_{BG} by including the amount of $60 \mu\text{m}$ intensity that exceeds what we expect from the VSGs, that is, the $60 \mu\text{m}$ emission above the dotted line in Figure 6. For H^+ in BL (top, bottom) we obtain $T_{\text{BG}} = (24.2, 22.4)$ K. These correspond to $b_{\text{H}^+} = (6.9, 4.2)$, which is much larger than the $b_{\text{H}^+} = 2$ estimate above. This can be reconciled by making the clumping factor $f \neq 1$. If the physical path length over which the H^+ is distributed is fixed at 40 pc , then $f \propto b_{\text{H}^+}^{-2}$; if $b_{\text{H}^+} = 2$, as we argue above, then we require $f = [(6.9, 4.2)/2]^2 = (11.9, 4.4)$ and the path lengths actually occupied by the H^+ in BL are $L \sim (4, 9) \text{ pc}$. This is a high degree of clumping, and we would expect to see considerable small-scale structure of the $\text{H}\alpha$ emission within BL. However, the image presented by Isope (1973) does not give this impression. We conclude

TABLE 3
GRAIN TEMPERATURES, $100 \mu\text{M}$ EMISSIVITY, AND HEATING RATES

Condition (1)	T_{BG} (K) (2)	b_{H^+} (3)	$\frac{T_{\text{BG}}}{T_{\text{G,H I}}}$ (4)
Global H I	18.3	1.0	1.0
H^+ with $60 \mu\text{m}$, top	24.2	6.9	5.4
H^+ with $60 \mu\text{m}$, bottom	22.4	4.2	3.4
H^+ without $60 \mu\text{m}$, top	19.6	1.7	1.5
H^+ without $60 \mu\text{m}$, bottom	20.3	2.2	1.9

NOTE.—Global H I temperatures are from our fit to the spectrum of Arendt et al. 1998; all temperature fits assume a v^2 emissivity law, so column (4) is proportional to the grain heating rate. In column (3), b_{H^+} is the $\lambda = 100 \mu\text{m}$ grain emissivity in the H^+ relative to that in H I.

that the enhanced 60 μm intensity in BL does *not* come from warm BGs.

We next consider the other alternative, namely, that the enhanced 60 μm comes from an enhanced population of VSGs. In this fit, we derive T_{BG} in the usual way, by including only the $\lambda \geq 100 \mu\text{m}$ data. For H^+ in BL (top, bottom) we obtain $T_{\text{BG}} = 24.2$ and 22.4 K. These correspond to $b_{\text{H}^+} = 1.7$ and 2.2, which agrees well with the $b_{\text{H}^+} = 2$ estimate above. These grains require an excess heating rate relative to global H I by factors of 1.5 and 1.9.

This excess heating rate is very close to that expected from the added heating by Ly α photons trapped in ionized gas. Spitzer (1978) shows that this mean intensity of these photons is $I_{\text{Ly}\alpha} \approx 1.1 \times 10^{-3} n_e \text{ ergs cm}^{-2} \text{ s}^{-1} \text{ sr}^{-1}$. The interstellar radiation field (ISRF) is equivalent to a blackbody at 3.14 K (Mathis, Mezger, & Panagia 1983), or $I_{\text{ISRF}} \approx 1.8 \times 10^{-3} \text{ ergs cm}^{-2} \text{ s}^{-1} \text{ sr}^{-1}$. For $n_e = 2 \text{ cm}^{-2}$ (§ 6.2), we have $(I_{\text{ISRF}} + I_{\text{Ly}\alpha})/I_{\text{ISRF}} = 2.3$, which is close to the excess heating obtained in the above paragraph.

We emphasize that this extra grain heating is a generally occurring process in all H^+ regions that trap Ly α photons (the “on-the-spot” case). The H^+ grain heating rate $\approx (1 + 0.6n_e)$ times larger than the H I grain heating rate. This translates into an increased IR emission per grain.

We much prefer this second alternative because it is consistent with the $b_{\text{H}^+} = 2$ estimate obtained from our geometrical argument in § 6.2. Also, the increase in T_{BG} is modest and is attained with something close to the expected increase in grain heating rate. We conclude that the 60 μm excess in the H^+ of BL comes from an enhanced population of VSGs.

In contrast, the relative 12 μm intensity from BL is smaller than that from the global H I. This result is strongly suggested from Figure 6 but, given the uncertainties, not absolutely certain. The 12 μm emission comes from a third population of grains; many workers, including Désert et al. (1990), believe they are PAHs. We conclude that, with high probability, the population of PAHs relative to BGs in the H^+ gas of BL is smaller than in global H I.

Our conclusions, then, are that the VSGs are more abundant and the PAHs less abundant in BL than in global H I. This is similar to but firmer than the results of Désert et al. (1990) on the H^+ gas in the California Nebula. Clearly, it would be desirable to confirm this trend by studying other H II regions.

8. CONCLUSIONS

In § 2, we derived the radio spectral index of Barnard's loop (BL) from large-scale radio surveys at four frequencies. We eliminated possible scale errors by assuming the H II region λ Ori to be a thermal (optically thin bremsstrahlung) radio source. We found BL to have a thermal spectrum, too.

Having found the radio emission of BL to be thermal, we could combine the radio and H α line data in § 3 to derive upper limits on the electron temperature (Table 1) for four regions: the λ Ori H II region, two regions in BL, and a high-latitude filament in the wall of the Orion-Eridanus

superbubble. In § 4 we discussed two of these regions in detail and compared our temperatures with those previously obtained from N II and H α line ratios. Our currently derived temperatures were lower than the previous ones. We developed a toy model to explore the effect of temperature structure along the line of sight, and found that one expects the radio/H α temperatures to be somewhat smaller than the N II/H α temperatures. However, most of the discrepancy is a result of inaccurate absolute intensity calibrations. Provisionally, we accepted the 2326 MHz radio survey calibration as accurate (Jonas et al. 1998) and ascribed all the error to the WHAM survey data, whose final calibration has not yet been done; the current WHAM intensities need to be multiplied by the factor of 0.89.

We discussed the four regions in some detail and adopted reddenings, which enabled us to derive actual electron temperatures (Table 1). Temperatures in all four regions are somewhat smaller than in the Orion Nebula and other H II regions near the Sun.

In § 6 we performed least-squares fits of the DIRBE diffuse IR intensities to the 21 cm line and radio continuum intensities. Our derived IR spectrum spans $\lambda = 12$ to 240 μm and agrees well with the spectrum from global H I derived by Arendt et al. (1998). In this fit, the ratio of the derived coefficients of the 21 cm line and radio continuum allow one to determine the electron density n_e . However, our derived n_e is small, requiring a very long path length through the H α -emitting region, which is inconsistent with the BL morphology and leads to the “geometrical conundrum” of § 6.2.

The conundrum can be resolved if the H^+ grains emit more IR per H nucleus than H I grains do. This, together with the modified IR spectrum from the H^+ gas, is explained in § 7 by a higher grain temperature in the H^+ than in the H I (T_{BG} in Table 3: H I is the first entry, H^+ the last two entries). The increased grain temperature in the H^+ gas agrees well with that expected from the extra heating produced by trapped Ly α photons. The H^+ grain heating rate is generally higher than the H I heating rate by a factor of $\approx (1 + 0.6n_e)$.

In BL, $n_e \approx 2.0 \text{ cm}^{-3}$ and $T \approx 6100 \text{ K}$. The pressure is $P/k \approx 24,000 \text{ cm}^{-3} \text{ K}$. In addition, the H^+ grains in BL exhibit excess 60 μm emission and deficient 12 μm emission, indicating that very small grains (VSGs) are more abundant and PAHs less abundant in BL than in the global H I.

We thank D. Finkbeiner for much pleasurable and instructive consultation and for supplying destriped versions of the IR and 408 MHz data sets in a convenient form; J. Jonas for a copy of his thesis, the 2326 MHz data set, and instructive discussions; P. and W. Reich for instruction and consultation on the three low-frequency radio continuum data sets; and C. Salter for discussions on the radio properties of BL. WHAM is supported by National Science Foundation grant AST 96-19424, and C. H. is supported in part by grant AST 95-30590.

REFERENCES

- Arendt, R. G., et al. 1998, ApJ, 508, 74
 Berkhuijsen, E. M. 1972, A&AS, 5, 263
 Binney, J., & Merrifield, M. 1998, Galactic Astronomy (Princeton: Princeton Univ. Press), 98
 Bohlin, R. C., Savage, B. D., & Drake, J. F. 1978, ApJ, 224, 132
 Désert, F.-X., Boulanger, F., & Puget, J. L. 1990, A&A, 237, 215
 Diplas, A., & Savage, B. D. 1994, ApJS, 93, 211
 Gaylard, M. J. 1984, MNRAS, 211, 149
 Haffner, L. M., Reynolds, R. J., & Tuft, S. L. 1999, ApJ, 523, 223
 Hartmann, D., & Burton, W. B. 1997, Atlas of Galactic Neutral Hydrogen (Cambridge: Cambridge Univ. Press)
 Haslam, C. G. T., & Salter, C. J. 1971, MNRAS, 151, 385

- Haslam, C. G. T., Salter, C. J., Stoffel, H., & Wilson, W. E. 1983, *A&AS*, 47, 1
- Heiles, C., Haffner, L. M., & Reynolds, R. J. 1999, in *ASP Conf. Ser. 168, New Perspectives on the Interstellar Medium*, ed. A. R. Taylor, T. O. Landecker, & G. Joncas (San Francisco: ASP), 211
- Isobe, S. 1973, in *Interstellar Dust and Related Topics (IAU Symp. 52)*, ed. M. Greenberg & H. Van de Hulst (Dordrecht: Reidel), 433
- . 1978, *PASJ*, 30, 499
- Jonas, L. J., Baart, E. E., & Nicolson, G. D. 1998, *MNRAS*, 297, 977
- Martin, P. G. 1988, *ApJS*, 66, 125
- Mathis, J. S. 1983, *ApJ*, 267, 119
- Mathis, J. S., Mezger, P. G., & Panagia, N. 1983, *A&A*, 128, 212
- Meyer, D. M., Cardelli, J. A., & Sofia, U. J. 1997, *ApJ*, 490, L103
- Meyer, D. M., Jura, M., & Cardelli, J. A. 1998, *ApJ*, 493, 222
- Mezger, P. G., & Henderson, A. P. 1967, *ApJ*, 147, 471
- O'Dell, C. R., York, D. G., & Henize, K. G. 1967, *ApJ*, 150, 835
- Osterbrock, D. E. 1989, *Astrophysics of Gaseous Nebulae and Active Galactic Nuclei* (Mill Valley, CA: Univ. Sci. Books)
- Reach, W. T., Wall, W. F., & Odegard, N. 1998, *ApJ*, 507, 507
- Reifenstein, E. C., Wilson, T. L., Burke, B. F., Mezger, P. G., & Altenhoff, W. J. 1970, *A&A*, 4, 357
- Reich, P., & Reich, W. 1986, *A&AS*, 63, 205
- . 1988, *A&AS*, 74, 7
- Reich, W. 1978, *A&A*, 64, 407
- Reynolds, R. J. & Ogden, P. M. 1979, *ApJ*, 229, 942
- . 1982, *AJ*, 87, 306
- Rubin, R. H. 1968, *ApJ*, 153, 761
- Schlegel, D., Finkbeiner, D. P., & Davis, M. 1998, *ApJ*, 500, 525
- Sembach, K. R., Howk, J. C., Ryans, R. S. I., & Keenan, F. P. 2000, *ApJ*, 528, 310
- Shaver, P. A., McGee, R. X., Newton, L. M., Danks, A. C., & Pottasch, S. R. 1983, *MNRAS*, 204, 53
- Savage, B. D., & Mathis, J. S. 1979, *ARA&A*, 17, 73
- Spitzer, L. 1978, in *Physical Processes in the Interstellar Medium* (New York: J. Wiley), 196